12th International Conference on Fracture Mechanics of Concrete and Concrete Structures
FraMCoS-12
B.L.A. Pichler, Ch. Hellmich, P. Preinstorfer (Eds)

https://doi.org/10.21012/FC12.1217
MS10-1:2

EFFECTS OF AGGREGATE FRAGMENTATION, FREE WATER AND STRAIN RATE ON FRACTURE IN COMPRESSIVE CONCRETE WITH A COUPLED DEM-CFD APPROACH

M. KRZACZEK[*], M. NITKA[*] AND J.TEJCHMAN[*]

[*] Gdańsk University of Technology, Civil Engineering and Environmental Faculty, Technische Narutowicza 11/12, 80-233 Gdańsk, Poland
e-mail: mkrzacze@pg.edu.pl, micnitka@pg.edu.pl, tejchmk@pg.edu.pl

Key words: Concrete, Aggregate Fragmentation, Strain Rate, Free Water, DEM-CFD

Abstract: The impact of aggregate fragmentation, free water, and strain rate content on the dynamic behavior of concrete under the uniaxial compression state at the mesoscale was examined in this study. Extensive two-dimensional (2D) dynamic investigations were conducted to examine the impact of aggregate fragmentation and strain rate on concrete's dynamic strength and fracture patterns. The behavior of fully and partially fluid-saturated concrete was simulated using a mesoscopic pore-scale hydro-mechanical model based on a unique fully coupled DEM/CFD approach wherein a DEM-based breakage model was used. Concrete was simulated as a four-phase material consisting of aggregate, mortar, ITZs, and macropores. The concrete mesostructure was obtained from laboratory micro-CT tests. Collections of small spherical particles were used to imitate aggregate breakage of different sizes and shapes by enabling intra-granular fracturing between them. The dynamic compressive strength increased with the strain rate, fluid saturation, and aggregate fragmentation.

1 INTRODUCTION

Concrete is sensitive to the strain rate. Strength, elastic (secant) modulus, and peak strain are all typically reported to rise with strain rate. An increase in the loading rate also causes the failure mechanism to alter. The strengths increase more quickly at a threshold strain rate, roughly 50 1/s for compression and 1 1/s for tension. With increasing strain rate, so does the cracking density. The increase in compressive strength is mostly caused by two phenomena: structural inertial forces, which produce radial inertial forces that are comparable to lateral confining pressure, and movement of viscous free water in micro-defects. The free water generates fluid confinement in pores and cracks which slows the fracture process and increases strength. Furthermore, for high strain rates aggregate fragmentation is also important. The cracks propagate through coarse aggregate instead of propagating along the weaker zones (mortar, ITZs) due to high-speed stress waves traveling fast through the specimen. Thus, the fragmentation process of the aggregate (typically stronger than the mortar in standard concrete) produces stronger concrete.

The concrete, dry or wet, under dynamic uniaxial compression, is the subject of the current numerical study. The goal of the study is to ascertain how aggregate fragmentation and free water migration qualitatively affect the partially saturated concrete behavior at the mesoscopic scale at various high strain rates, changing mainly between 1 1/s and 100 1/s as compared to the quasi-static response. Through a series of numerical simulations with a unique fully coupled DEM/CFD approach

[1]-[5], the impacts of aggregate fragmentation, fluid saturation, fluid viscosity, and strain rate on a stress-strain curve fracture mechanism, and pore pressure were examined. The focus was on fluid flow changes in pores and cracks and their influence on internal stresses. The solid-fluid interaction at the mesoscale was investigated using a fully coupled hydro-mechanical. The proposed model considers the two-phase (water and air) laminar viscous flow of immiscible and compressible fluid through pores and cracks in a continuous domain between discrete elements. The flow network, which is comprised of pre-defined channels, is represented by CFD. Compared to the other DEM-CFD models in the literature, it offers the following advantages:

1. Direct numerical simulation is the method used to solve fluid flow equations.
2. The discrete solid domain and the continuous fluid domain are both included in one physical system.
3. Both domains are discretized under 2D conditions to produce a single triangular mesh. Because the mesh takes into account the different shapes, sizes, locations, and volumes of the pores/cracks, it is possible to track the liquid/gas content in the pores and cracks with accuracy.
4. An efficient technique is created to automatically mesh and re-mesh the particle and fluid domains to accommodate topological and geometric changes.
5. The solid and liquid domain coarse meshes are used to build a virtual fluid flow network.
6. The two-phase immiscible fluid in porous materials comprises a liquid (water) and a gas (air).

To cut down the computation time, the 2D model in isothermal settings was used in the initial research stage. Concrete was simulated as a four-phase material consisting of aggregate, mortar, ITZs, and macropores. The concrete mesostructure was obtained from laboratory micro-CT tests. A so-called clump breakage algorithm [6] was applied to imitate intra-granular fragmentation of aggregates. Clumps composed of small spheres were used to describe the aggregate particles of different diameters and shapes.

2. 2D DEM/CFD-BASED MODEL

DEM for cohesive-frictional materials

Numerical analyses were performed using YADE [7], a 3D open-source DEM program that takes advantage of the so-called soft-particle approach (i.e. the DEM model allows for particle deformation that is simulated as an overlap of particles) (Fig.1). Particles in DEM interact with one another during translational and rotational motions with the application of an explicit time-stepping technique and Newton's second law of motion. An overlap between two contacted bodies is allowed. Due to the particle overlap, any micro-porosity may be reached. Because DEM takes into account inertial forces, it is a dynamic technique. The model predicts a cohesive bond at the grain contact with a brittle failure below the critical normal tensile force. Shear cohesion failure under typical compression results in contact stick and slip being governed by the Coulomb friction law. If a cohesive joint between two elements vanished after crossing a critical threshold, damage was presumed. If any contacts between spheres were restored following failure, there was no cohesion. The DEM model did not account for material softening. The model was successfully used by the authors to represent the behavior of numerous engineering materials having a particulate structure, such as granulates [8], concrete [9], [10], reinforced concrete [11], and rocks [12].

The following material constants are required for DEM simulations: E_c, (elastic modulus of the grain contact), υ_c (Poisson's ratio of the grain contact), μ_c (inter-particle friction angle), C (cohesion at the contact), and T (tensile strength of the contact). Additionally necessary are the parameters R (particle radius), ρ (mass density), and α_d (damping coefficient) As the C/T ratio grows, a more brittle and tensile failure mode dominates, and more tensile cracks appear [12]. Typically, the material constants in DEM are determined by running several simulations and comparing the

outcomes to experimental data from simple tests, such as uniaxial compression, triaxial compression, and simple shear.

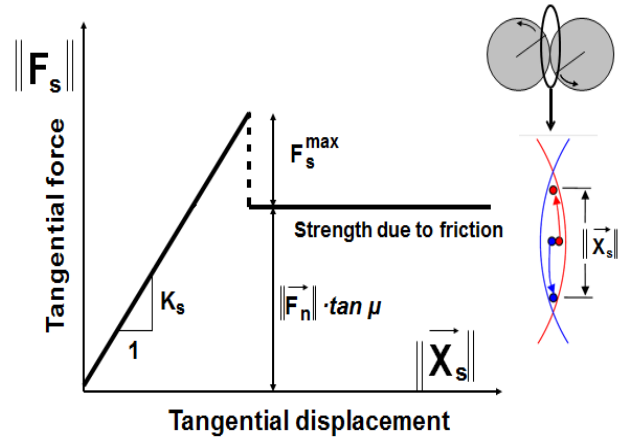

a)

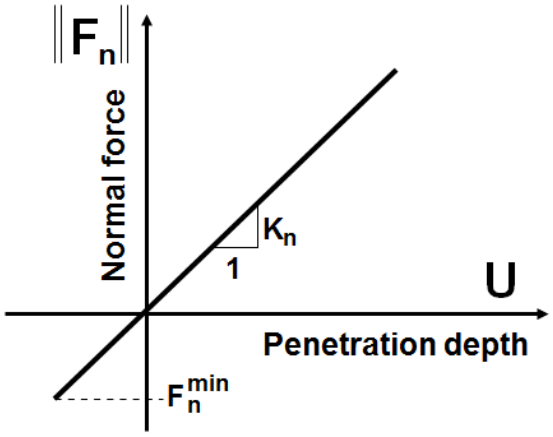

b)

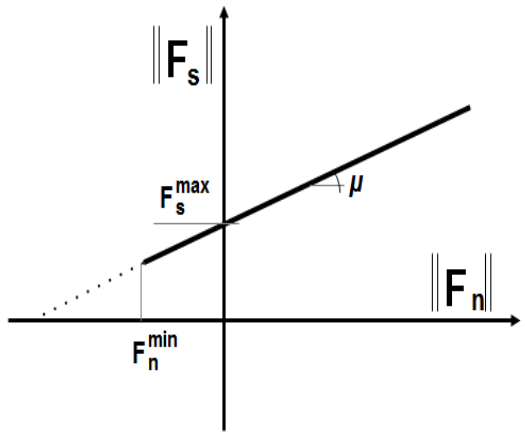

c)

Figure 1: Mechanical response of DEM: a) tangential contact model, b) normal contact model, c) modified Mohr-Coulomb model [7]

CFD model

A discrete 3D domain (solid) and a continuous 2D domain (fluid) coexisted in one physical system in the authors' 2D DEM-CFD model (Fig.2) [1], [2]. Triangular meshes were automatically generated by the meshing/remeshing procedures in both domains. The operation was started if one or more discrete elements were moved further than the designated maximum distance. First, a two-dimensional set of points was generated. Points were produced in the spaces between discrete elements along contact edges and along discrete elements themselves. The first convex object mesh was then produced by applying Delaunay triangulation techniques. The mesh was then improved using the Alpha Shapes theory to replicate the geometry (such as concave pores) more accurately. The mesh that was generated was passable in quality, albeit coarse. The following step was completing the identification procedure, which categorized each mesh element into a solid or fluid domain. In the final step, the computing results from the prior mesh were transferred to the current mesh using remeshing, assuming that the mass was a topological invariant. The fluid domain and the solid domain were the two remaining 2D domains following projection and discretization. It should be noted that the spheres' motion was fixed in an OZ's direction, perpendicular to the plane. Thus, even with the use of YADE's 3D DEM solver, the mechanical problem was functionally 2D, similar to the fluid flow model. The CFD model, which had a unit size in its third dimension, treated all definitions pertinent to the geometry of the two domains (fluid and solid) as two-dimensional.

Two distinct channel types were established [1], [2] (Fig.2):

A) artificial "S2S" channels linking discrete elements that are in contact with one another and

B) actual "T2T" channels that connect grid triangles in pores that are in contact with one another along a common edge.

The numerical algorithm was divided into four main phases:

1) mass flow rate for each phase of fluid flowing through the cell faces (in channels surrounding virtual pores) was calculated by solving momentum and continuity equations,
2) phase fractions and their densities in virtual pores were determined using equations of state and continuity,
3) pressure in virtual pores was obtained from the equation of state, and
4) material properties (such as liquid and gas densities in each cell grid) were updated.

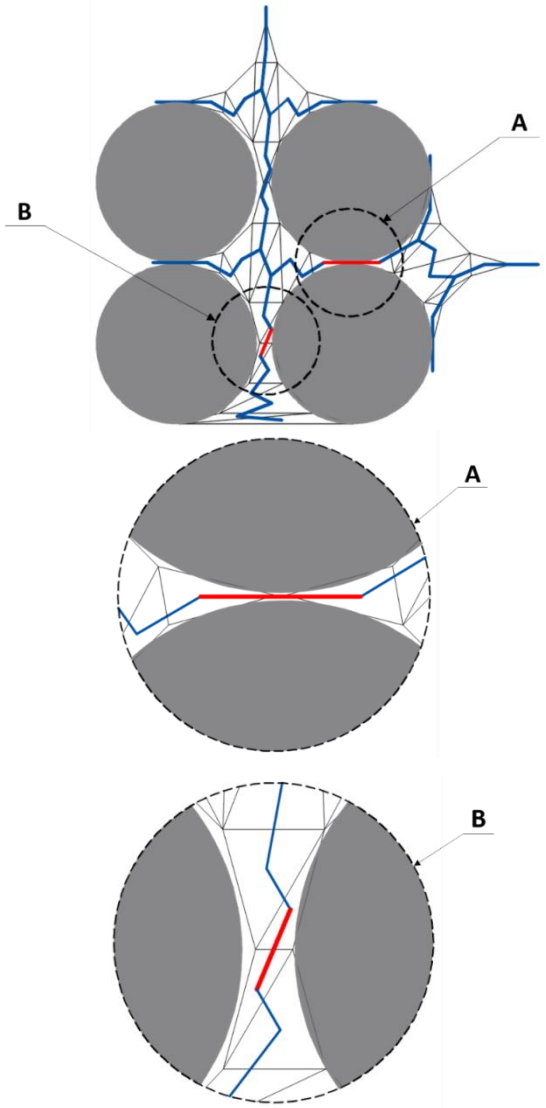

Figure 2: Fluid flow network in rock matrix with triangular discretization of pores (in blue): A) artificial channel type 'S2S' (red colour) and B) actual channel type 'T2T' (red colour) [1], [2]

3. INPUT DATA FOR 2D DEM/CFD APPROACH

A square concrete specimen 50 × 50 mm^2 geometry was assumed in 2D analyses. The depth of the specimen was equal to the grains' diameter. The bottom boundary was vertically fixed. Vertical boundaries were free and horizontal boundaries were smooth to eliminate a size effect due to wall friction. A constant vertical velocity v was applied along the upper horizontal boundary to deform the specimen (as during a standard uniaxial compression test).

Concrete was modeled as a four-phase material composed of mortar, aggregate, ITZs, and macro-pores. The porous ITZs surrounding aggregate particles were characterized as weaker contacts that lacked a defined physical width [9]. The macropores in the mortar (only with a diameter ≥1 mm) were modeled as empty regions of circular shape [9]. The aggregate's range in concrete was d=1-16 mm. Based on micro-CT images, the mesostructure was presumed to be from the actual concrete specimen. The aggregate's range on the micro-CT image d=1-8 mm. The clusters of 0.25-0.50 mm diameter spheres were always used to create the aggregate particles (independently of their size) for faithfully reproducing their real shapes. The spheres with diameters of 0.25-0.50 mm were also used to simulate the mortar particles. The effect of d_{min} in the mortar on the stress-strain curve in quasi-static DEM simulations was negligible if d_{min} was small enough, i.e. d_{min}≤0.25-0.50 mm. The specimen's initial porosity was p=5%.

In DEM simulations, we assumed the material constants in the mortar similar to the previous analyses of concrete fracture [8]. In the case of ITZs, the ratio $E_{c,ITZ}/E_{c,cm}$=0.70 was chosen [9], based on the nanoindentation experiments. The remaining two ratios in ITZs, C_{ITZ}/C_{cm} and T_{ITZ}/T_{cm}, were also assumed to be equal to 0.70 due to a lack of experimental data for mortars of different initial porosity. Based on triaxial compression tests with clumped granulates, the inter-particle friction angle of μ_c=18^o was postulated

[8]. The damping factor was mainly set to α_d=0.05 (approximately equal to the material damping of concrete). A total of 30,000 spherical elements were used, with 18,000 elements modeling mortar and 12,000 elements modeling aggregate.

Permeability and sorptivity testing (CFD) are typically used to calibrate CFD [13]. A square non-deformable specimen with a size of 10×10 mm^2 was used for permeability 2D simulations using pure CFD. According to Darcy's law, the concrete specimen's macroscopic permeability coefficient κ was determined to be 4.0×10^{-16} m^2 So, in numerical computations, an arbitrary permeability coefficient may be assumed. DEM and CFD always have a set adaptive time step [1], [2]. There was a maximum time step restriction of 1×10^{-8} s.

4. PURE DEM RESULTS

Figures 3 and 4 demonstrate the pure 2D DEM results with breakable aggregate for a dry concrete specimen with varying strain rates (0.1/s≤$\dot{\epsilon}$≤1000 1/s) and different mortar parameters [6]. The dynamic stress-strain curves are shown in Fig.3 (σ=f(ε_y), where σ - vertical normal stress and ε_y - vertical normal strain). Figures 1a and 1c include the stress-strain curves for $\dot{\epsilon}$≤100 1/s and Fig.3b also for $\dot{\epsilon}$≤1000 1/s. The static/dynamic compressive strength was calculated as the mean maximum vertical normal force calculated along the top and the bottom divided by the specimen area (width times depth). The vertical normal strain was calculated as the displacement increment related to the initial specimen height (engineering strain). Figure 4 presents the fracture patterns (based on displacements) in the deformed specimens at the failure).

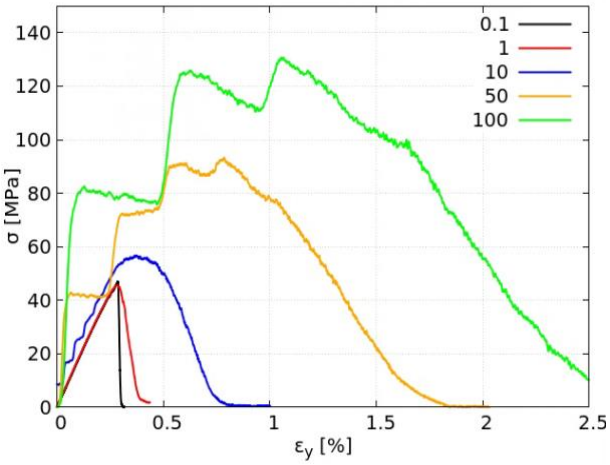

a)

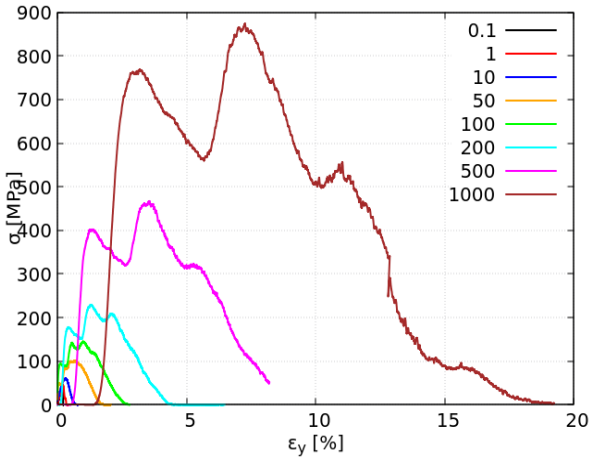

b)

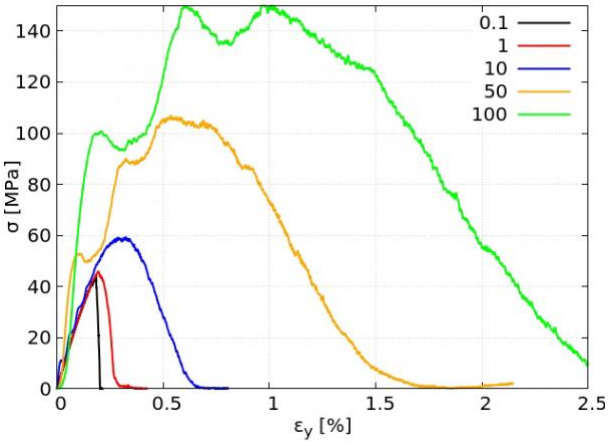

c)

Figure 3: DEM results: relationship between vertical normal stress σ and vertical normal strain ε_y for different strain rates (0.1/s ≤$\dot{\epsilon}$≤ 1000 1/s) with various breakable aggregate properties: a) mortar parameters multiplied by factor 2, b) mortar parameters multiplied by factor 5, and c) mortar parameters multiplied by factor 10 [6].

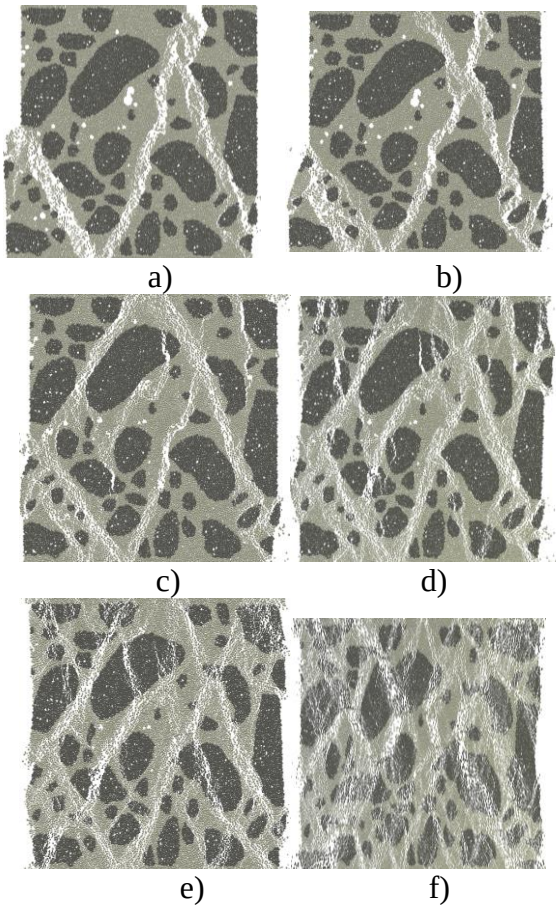

FIGURE 4: DEM displacement results with aggregate breakage: evolution of fracture at failure for different strain rates (50 1/s≤ $\dot{\epsilon}$ ≤1000 1/s) with mortar parameters multiplied by factor 5 (displacements are magnified by factor 2, macropores are marked as white spots): a) $\dot{\epsilon} = 0.1$ 1/s, b) $\dot{\epsilon} = 1\,1/s$, c) $\dot{\epsilon} = 10$ 1/s, d) $\dot{\epsilon} = 50$ 1/s, e) $\dot{\epsilon} = 100$ 1/s, and f) $\dot{\epsilon} = 1000$ 1/s [6].

The concrete compressive strength, elastic modulus, vertical strain corresponding to the strength, and post-peak toughness strongly raised with increasing strain rate as in the experiments (Fig.3). The material softening rate slightly raised for $\dot{\epsilon}$<0.10 1/s and later for $\dot{\epsilon}$≥0.10 1/s With a vertical normal strain of between ε_y=0.18% and ε_y=0.28%, the predicted dynamic compressive strength was f_c=44-47 MPa and the global elastic modulus was E=20-30 GPa for the strain rate $\dot{\epsilon}$=0.1 1/s. For $\dot{\epsilon}$=100 1/s, the predicted dynamic compressive strength was estimated as f_c=130-150 MPa with a vertical normal strain of roughly ε_y=1% and the elastic modulus was E=50-100 GPa (Fig.3). The mean compressive strength's growth (based on DEM simulations with three different aggregate strengths) was, thus, about 3. The stress oscillations in the pre-peak regime due to the wave dispersion and reflection raised with increasing strain rate in contrast to SHPB tests where they were negligible. For $\dot{\epsilon}$=1000 1/s, the mean strength's growth was already about 18 (Fig.3b), i.e. too high as compared with SHPB experiments. The vertical normal strain corresponding to the strength was also too high.

The crack patterns in the concrete specimen were composed mainly of variously inclined cracks (Fig.4). The cracks occurred in the entire specimen. Their number increased with the growing strain rate. For $\dot{\epsilon}$≤10 1/s, they were successively created in the weak ITZs (ε_y=0.1%), mortar (ε_y=0.15%), and breakable aggregate (ε_y=0.25-0.5%). For $\dot{\epsilon}$=100 1/s and $\dot{\epsilon}$≤1000 1/s, the cracks started to co-occur in ITZs, mortar, and aggregates. For very high strain rates ($\dot{\epsilon}$=1000 1/s), the specimens were almost totally fractured as in the experiments. The fracture patterns were similar for the strain rates $\dot{\epsilon}$=0.1 1/s and $\dot{\epsilon}$=1 1/s (Fig.4). At the stress peak, several cracks were already created for $\dot{\epsilon}$≥10 1/s only. However, many cracks already occurred at this moment for $\dot{\epsilon}$=1000 1/s. Cracks in the aggregate appeared even in a quasi-static regime when the aggregate was twice as strong as the mortar. Such a phenomenon also occurs in quasi-static laboratory experiments with the usual aggregate. For the aggregate ten times stronger than the mortar, macro-cracks started to form in the aggregate from $\dot{\epsilon}$=50 1/s.

5. COUPLED DEM-CFD RESULTS

Figure 5 presents a relationship between the vertical normal stress σ_y and vertical normal strain ε_y for a dry and fully saturated specimen with unbreakable aggregate and two different strain rates of $\dot{\epsilon}$=50 1/s and $\dot{\epsilon}$=100 1/ [5]. The evolution of average pore fluid pressures against vertical normal strain ε_y is shown for the wet specimen (α_q=1.0) with two different strain rates in Fig.6.

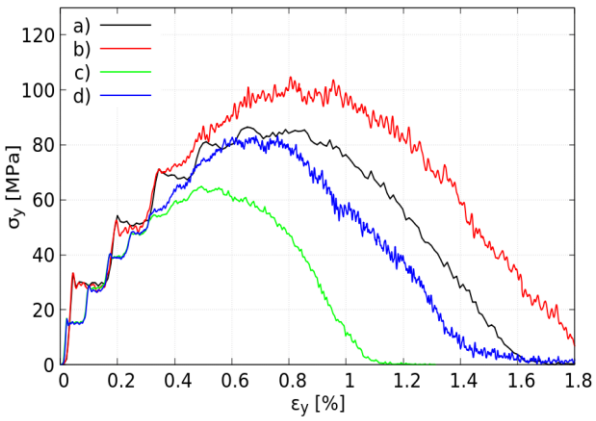

Figure 5: Pure DEM and DEM-CFD simulation results for one-phase concrete specimen with unbreakable aggregate during dynamic uniaxial compression: relationship between vertical normal stress σ_y and vertical normal strain ε_y: a) pure DEM $\dot{\epsilon}$=100 1/s, b) DEM-CFD with α_q=1.0, $\dot{\epsilon}$=100 1/s, c) pure DEM $\dot{\epsilon}$=50 1/s, and d) DEM-CFD with α_q=1.0, $\dot{\epsilon}$=50 1/s [5].

The concrete strength grew with increasing strain rate: f_c=63 MPa (ε_y=0.50%) for the dry specimen, f_c=80 MPa (ε_y=0.65%) for the wet specimen with $\dot{\epsilon}$=50 1/s, and f_c=83 MPa (ε_y=0.65%) for the dry specimen and f_c=105 MPa (ε_y=0.80%) for the wet specimen with $\dot{\epsilon}$=100 1/s. For the fully saturated specimens, the vertical normal strain was 30% higher and the compressive strength was 25% higher than the results for a dry specimen for $\dot{\epsilon}$=50 1/s, and the vertical normal strain was 20% higher and the compressive strength was 25% higher than the results for a dry specimen for $\dot{\epsilon}$=100 1/s. The elastic moduli slightly rose with increasing $\dot{\epsilon}$. The softening rate was similar to the experiments. The post-peak toughness increased due to the growing strength. The damage pattern was similar for two different strain rates.

The evolutions of the average pore fluid (air and water phase) pressures (Fig.6) in the fully saturated specimens were similar as for $\dot{\epsilon}$=10 1/s. First, they marginally increased with expanding strain up to 0.1002 MPa and then they diminished and reached a residual state for 0.10004 MPa. The maximum average pore fluid velocities were about v=0.0032 m/s ($\dot{\epsilon}$=50 1/s) and v=0.0031 m/s ($\dot{\epsilon}$=100 1/s). They were slightly lower than for $\dot{\epsilon}$=10 1/s (v=0.04 m/s).

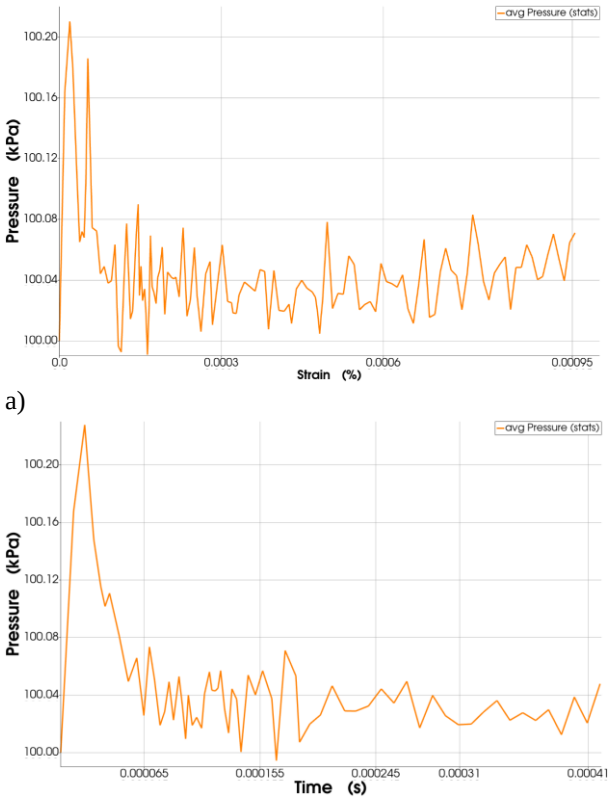

Figure 6: Coupled DEM-CFD results for fully fluid-saturated concrete specimen (α_q=1.0) with unbreakable aggregate: evolution of average pore fluid pressure [Pa] against vertical normal strain ε_y during dynamic uniaxial compression (a) $\dot{\epsilon}$=50 1/s and b) $\dot{\epsilon}$=100 1/s) [5].

Figure 7 summarizes the findings and illustrates how the saturation grade and compressive strength relate to each other at various strain rates without aggregate fragmentation. For $\dot{\epsilon}$ =10 1/s, the compressive strength increased linearly with the saturation grade. It can be inferred that a linear increase also took place for $\dot{\epsilon}$=50 1/s and $\dot{\epsilon}$=100 1/s. The strength increase became higher with the growing strain rate.

The dynamic increase factor (DIF) is the ratio of dynamic compressive strength to quasi-static compressive strength (usually shown on a logarithmic scale of $\dot{\epsilon}$). It is commonly used to explain how strain rate influences the dynamic mechanical properties of cement-based materials. It is determined

with a split Hopkinson pressure bar (SHPB) test.

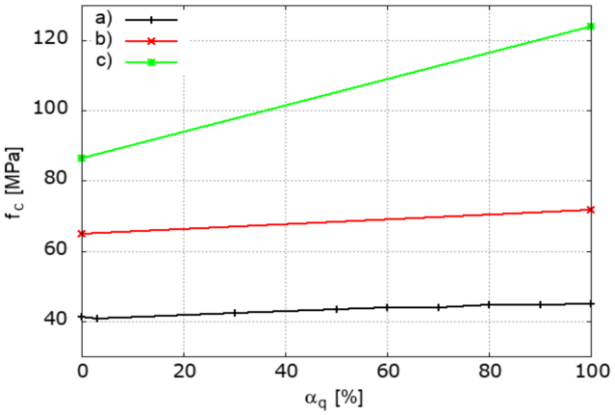

Fig.7: Coupled DEM-CFD results with unbreakable aggregate: compressive strength f_c against initial fluid volume fraction α_q for three different strain rates $\dot{\epsilon}$: a) $\dot{\epsilon}$=10 1/s, b) $\dot{\epsilon}$=50 1/s, and c) $\dot{\epsilon}$=100 1/s [5].

By maintaining the dynamic force balance, the SHPB test currently emerged as a popular laboratory instrument for examining the mechanical characteristics of materials such as rock, ceramic, mortar, and concrete under high-speed non-shock load impacts for $\dot{\epsilon}$>10 1/s [14], [15]. A drop-weight impactor or hydraulic servo testing device may be employed below this strain rate. The assumptions of homogeneity and one-dimensional stress waves are essential to the data analysis of the SHPB test. The very long metal bars (incident bar and transmission bar) guarantee the assumption of 1D stress wave propagation. The homogeneity of the material is ensured by large bar diameters equal approximately to the specimen one. Because of the obvious discrepancies between the two loading systems, the DEM uniaxial compression results were only qualitatively compared with the experimental literature data from SHPB testing.

The numerical values of DIF for concrete with unbreakable aggregate are depicted against the strain rates in Fig.8 on a logarithmic scale (between -2 and 2). The dry static strength was f_c=36 MPa [3]. The strength non-linearly increased with the growing strain rate. The increase was pronounced for $\dot{\epsilon}$>1.0 1/s. The values of DIF in the DEM/DEM-CFD simulations (α_q=1) were: 1.1/1.2 ($\dot{\epsilon}$=10 1/s), 1.8/2.2 ($\dot{\epsilon}$=50 1/s) and 2.3/2.9 ($\dot{\epsilon}$=100 1/s) (Fig.8). The calculated curve DIF=f(log($\dot{\epsilon}$)) from DEM-CFD analyses resembled the one assumed in CEB-FIP [16], based on laboratory SHPB outcomes: However, all the calculated DIF values by DEM-CFD were higher than those given in [12]: 1.2 ($\dot{\epsilon}$=10 1/s), 1.4 ($\dot{\epsilon}$=50 1/s) and 1.8 ($\dot{\epsilon}$=100 1/s). The same growing trend of DIF was also obtained in calculations for the higher strain rate $\dot{\epsilon}$>100 1/s (not shown here).

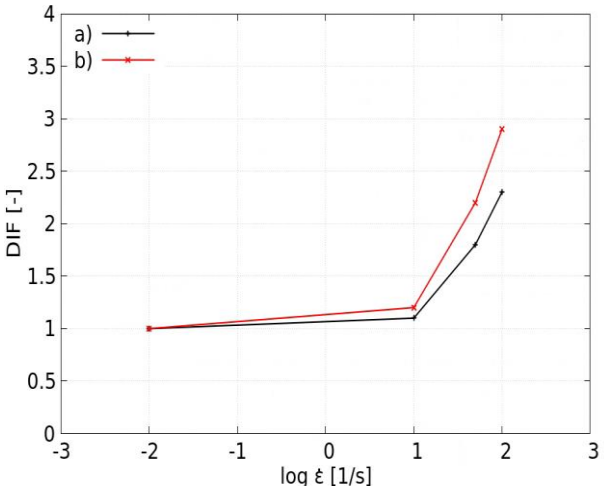

Figure 8: Dynamic impact factor DIF during compression against logarithmic strain rate (log$\dot{\epsilon}$) for fully saturated specimen without aggregate fragmentation (α_q=1.0): a) pure DEM results and b) coupled DEM-CFD results [5].

Next, the coupled DEM-CFD simulations were performed with breakable aggregate wherein the mortar parameters were multiplied by factor 2. The numerical values of DIF are depicted versus the strain rates in Fig.9 on a logarithmic scale (between 0 and 2). The findings indicate that DIF was further raised by aggregate fragmentation. For e.g. $\dot{\epsilon}$=100 1/s, DIF=4.6 (with aggregate fragmentation) and DIF=2.4 (without aggregate fragmentation). The concrete's compressive strength increased since the fracture process was retarded by the fluid confinement in the mortar and aggregate cracks.

The strength differences between the numerical and experimental results in CEB-

FIP [16] are caused by different loading systems, specimen geometries and shapes, and concrete mesostructures assumed in experiments (SHPB compressive tests) and numerical analyses (2D uniaxial compression). The specimen deformation in SHPB testing, where long metal bars ensure 1D stress wave propagation, is substantially more uniform than in 2D DEM models, particularly at higher strain rates.

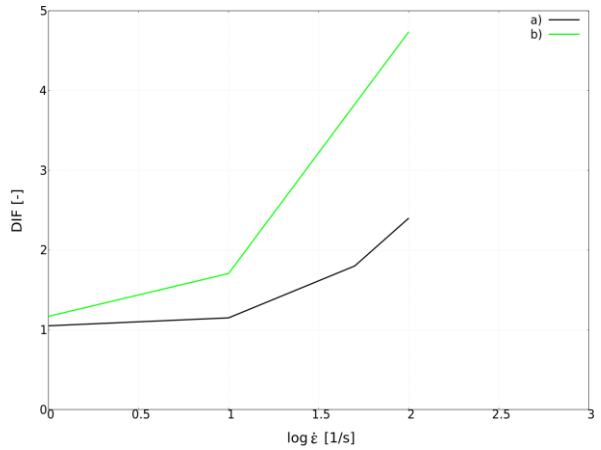

Figure 9: Dynamic impact factor (DIF) against logarithmic strain rate with aggregate parameters (mortar parameters multiplied by factor 2) from DEM-CFD simulations: a) aggregate fragmentation and no free water flow and b) aggregate fragmentation and free water flow.

12 CONCLUSIONS

The following findings of the 2D mesoscopic simulations of concrete specimens under dynamic uniaxial compression can be offered:

The strain rate significantly impacted the concrete's mechanical response following the existing literature research outcomes. The concrete compressive strength, elastic modulus, peak strain corresponding to the strength, and post-peak toughness strongly increased with increasing strain rate, exhibiting a notable strain rate strengthening effect as in experiments. The material softening rate initially rose with the strain rate (up to $\dot{\epsilon}$=10 1/s) and later remained similar.

- The concrete strength dropped with the fall of the strength of the breakable aggregate in the considered strength range. The drop was only 0.5% in quasi-static calculations and increased in dynamic calculations, up to 15% with $\dot{\epsilon}$=1000 1/s.

The patterns of cracks consisted of many inclined cracks. The cracks propagated throughout the entire specimen including aggregate particles. For low strain rates, the fracture process varied between cracks (but not fragmentation), and for huge strain rates ($\dot{\epsilon}$=1000 1/s), it underwent complete pulverization. As the strain rate increased, the specimen cracking grew. The damage rate, based on the evolution of broken contacts, non-linearly increased (approximately parabolically). The ITZs, mortar, and breakable aggregate all developed cracks one after the other for $\dot{\epsilon}\leq$10 1/s. For huge strain rates, they started to co-occur from the beginning of deformation. Even in the quasi-static tests, cracks were seen in the breakable aggregate.

The DEM-CFD calculations provided new insights into the effect of viscous free water on compressive response of concrete with low porosity at the mesoscopic scale for different strain rates. The numerical results were qualitatively in agreement with the corresponding experiments in the literature.

Free water and inertial forces had notable effects on the concrete response. Concrete's dynamic compressive strength increased consistently with strain rate, fluid saturation, and fluid dynamic viscosity (the strain rate had the greatest effect). The dynamic compressive strength increased linearly with fluid saturation and viscosity increases, but it grew nonlinearly with increases in strain rate.

Because there was insufficient time for the fluid to move through the pores and cracks in the concrete, the mesostructure prevented fluid migration during dynamic loading. The higher the strain rate, the less time the water migrated through pores and cracks. The fluid confinement in the pores/cracks retarded the fracture process and increased the compressive strength. Because of the decreased fluid migration through pores and fractures, the pore fluid pressure thus had a beneficial stiffening

effect on the material strength and damage rather than a negative one as during quasi-static compression. Higher contact forces and faster material damage were caused by the fluid's quasi-static flow through pores and cracks (dry concrete structures are thus more prone to failure).

The compressibility of fluid phases affected the dynamic compressive strength more than viscous fluid flow in contrast to the quasi-static tests.

Additionally, the aggregate fragmentation increased DIF.

REFERENCES

[1] Krzaczek, M., Kozicki, J., Nitka, M. and Tejchman, J., 2020. Simulations of hydro-fracking in rock mass at meso-scale using fully coupled DEM/CFD approach. *Acta Geotechnica* **15**(2), 297-324.

[2] Krzaczek, M., Nitka, M. And Tejchman, J., 2021. Effect of gas content in macro-pores on hydraulic fracturing in rocks using a fully coupled DEM/CFD approach. *Int J Numer Anal Methods Geomech,*, **45**(2), 234-264.

[3] Krzaczek, M., Tejchman, J. and Nitka, M., 2024. Effect of free water on the quasi-static compression behaviour of partially-saturated concrete with a fully coupled DEM/CFD approach. *Granular Matter.* **26**:38.

[4] Krzaczek, M. Tejchman, and Nitka M., 2024. Coupled DEM/CDF analysis of impact of free water on the static and dynamic response of concrete in tension regime. *Computers and Geotechnics* **172**, 106449.

[5] Krzaczek, M., Tejchman, J., and Nitka, M., 2024. Impact of free water on strain rate response of concrete in compression with a fully coupled DEM/CFD approach. *Computational Particle Mechanics*, (accepted).

[6] Nitka, M. and Tejchman, J., 2025 Effects of aggregate crushing and strain rate on fracture in compressive concrete with a DEM-based breakage model. *Granular Matter* **27**(8), doi: 10.1007/s10035-024-01487-3.

[7] Kozicki J., and Donze F.V., 2008. A new open-source software developer for numerical simulations using discrete modeling methods. *Computer Methods in Applied Mechanics and Engineering* **2197**, 4429-4443.

[8] Kozicki, J. and Tejchman, J. 2018. Relationship between vortex structures and shear localization in 3D granular specimens based on combined DEM and Helmholtz-Hodge decomposition. *Granular Matter* **20**, 48.

[9] Nitka, M. and Tejchman, J., 2018. A three-dimensional meso scale approach to concrete fracture based on combined DEM with X-ray μCT images. *Cement and Concrete Research* **107**, 11-29.

[10] Nitka, M. and Tejchman, J. 2020. Meso-mechanical modelling of damage in concrete using discrete element method with porous ITZs of defined width around aggregates. *Engineering Fracture Mechanics* **231**, 107029.

[11] Nitka, M. and Tejchman, J. 2024. Mesoscopic simulations of a fracture process in reinforced concrete beam in bending using a 2D coupled DEM/micro-CT approach. *Engineering Fracture Mechanics* **2304**,110153

[12] Tomporowski, D., Nitka, M. and Tejchman, J. 2023. Application of the 3D DEM in the modelling of fractures in pre-flawed marble specimens during uniaxial compression. *Engineering Fracture Mechanics* **277**, 108978.

13] Krzaczek, M., Nitka, M. and Tejchman, J., 2023. Modelling hydraulic and

capillary-driven two-phase fluid flow in unsaturated concretes at the meso-scale with a unique coupled DEM-CFD technique. *Int J Numer Anal Methods Geomech.* **47**(1): 23-53.

[14] Grote, D.L., Park, S.W., Zhou, M., 2001. Dynamic behavior of concrete at high strain rates and pressures: I. experimental characterization. *Int J Impact Eng* **25**(9):869–8.

[15] Li, X.Q., Chen, Q.J., Chen, J.F., Liao, J.Z. and Lu, Y., 2022. Dynamic increase factor (DIF) for concrete in compression and tension in FE modelling with a local concrete model. *International Journal of Impact Engineering* **163**, 104079.

[16] Fib Model Code for concrete structures, 2013. Lausanne: international Federation for Structural Concrete.